LIMNOLOGY AND OCEANOGRAPHY
Letters

ASLO
Open Access

Limnology and Oceanography Letters 2021

doi: 10.1002/lol2.10221

LETTER

Seasonal particle responses to near-bed shear stress in a shallow, wave- and current-driven environment

Grace Chang,[1]* *Galen Egan*,[2,3]* *Joseph D. McNeil*,[4] *Samuel McWilliams*,[1] *Craig Jones*,[1] *Frank Spada*,[1] *Stephen Monismith*,[2] *Oliver Fringer*[2]

[1]Integral Consulting Inc., Santa Cruz, California; [2]Department of Civil and Environmental Engineering, Stanford University, Stanford, CA; [3]Sofar Ocean Technologies, Inc., San Francisco, California; [4]Environmental Engineering and Limnological Services, Santa Barbara, California

Scientific Significance Statement

Effective management of sediment in aquatic systems is important for many environmental and societal issues and requires accurate models of sediment transport. Accurate sediment transport models require knowledge about properties of sediment: its composition, size, and concentration in the water column. These properties change based on how much force, or shear stress, is applied to the sediment bed. We show that by investigating relationships between acoustically derived shear stress and optically derived sediment properties, we can identify a characteristic shear stress, that is, a forcing at which the rate of change to sediment properties is most pronounced. Our results show that this characteristic shear stress varies seasonally and may be more important for sediment transport models as compared to the commonly applied critical shear stress for erosion.

Abstract

Novel analysis of in situ acoustic and optical data collected in a shallow, wave- and current-driven environment enabled determination of (1) particle characteristics that were most affected by near-bed physical forcing over seasonal scales and (2) characteristic shear stress, τ_{char}, at which the rate of change to particle characteristics was most pronounced. Near-bed forcing and particle responses varied by season. Results indicated that moderate τ_{char} values of 0.125 Pa drove changes in particle composition during summer. In winter, particle concentration effects were most affected at τ_{char} of 0.05 Pa, suggesting dominance of fluff layer resuspension. Changes to particle size were most relevant during a biologically productive springtime period, with initiation of particle disaggregation occurring most commonly at τ_{char} of 0.25 Pa. These results suggest that it may be more important to parameterize τ_{char}, as opposed to critical shear stress for erosion, for sediment transport models.

Contaminated bottom sediment and associated degradation of water quality is a major environmental problem affecting many of the world's aquatic systems. Understanding of benthic boundary layer sediment dynamics is therefore of

*Correspondence: gchang@integral-corp.com, gegan@stanford.edu

Associate editor: Jill S. Baron

Author Contribution Statement: GC, GE, CJ, SM, and OF developed the research question and designed the study approach. GC, GE, JM, SMc, CJ, FS, and OF discussed the analysis methods and outlined this manuscript. GC, GE, SMc, FS, and OF designed and/or conducted the field study. GC processed and analyzed optical data. GE processed and analyzed physical data, advised by SM and OF. GC wrote the paper and all authors reviewed and provided edits.

Data Availability Statement: All field data used in this paper are available in the Dryad repository at https://doi.org/10.5061/dryad.8sf7m0cpn.

utmost importance to quantification of the fate and transport of sediment and associated contaminants (e.g., Lick 2009; James et al. 2010). Knowledge of fate and transport of sediment is also essential for effective management of myriad environmental and societal issues including coastal resilience in the face of climate change. To effectively implement sediment transport models, it is necessary to accurately parameterize sediment bed erosion rates, which are dependent on near-bed shear stress and the properties of sediment such as bulk density, particle size, and composition (Roberts et al. 1998; Winterwerp et al. 2012).

The purpose of this paper is to describe a novel and relatively simple method of identifying characteristic shear stress that can provide limits on the range of shear stress values important to sediment transport models. We apply this method to an extensive in situ physical and optical data set collected over seasons that exhibit very different physical processes and particle properties. The effects of near-bed shear stress on particle size, concentration, and composition (minerogenic vs. organic) are described for the shallow, wave- and current-driven shoals of South San Francisco Bay (SF Bay), California, over seasonal scales. Our extensive physical-biooptical data set enabled us to address the following questions: (1) Which particle characteristic(s) (i.e., size, concentration, and composition) is/are most sensitive to near-bed physical forcing? (2) Can we derive a characteristic shear stress, τ_{char}, that is, the shear stress at which particles begin to resuspend or disaggregate, from our measurements? How do derived values of τ_{char} compare to the more commonly applied parameter, critical shear stress for erosion (τ_{cr}), in sediment transport models?

Materials and methods

Field experiments

We conducted a series of three field experiments on the shallow (1.5 m mean lower low water; 2 m tidal range) eastern shoals of South SF Bay to investigate boundary layer dynamics and effects on cohesive sediment processes and properties (Egan et al. 2019, 2020*a*,*b*, 2021). Experiments were conducted in summer (17 Jul 2018–15 Aug 2018; S18), winter (10 Jan 2019–07 Feb 2019; W19), and spring (17 Apr 2019–15 May 2019; Sp19) to measure a diverse set of dry, stormy, and biologically productive conditions. We deployed moored, bottom-mounted instrumentation at four measurement locations along a 5 km east– west transect. Here, data are presented from the central deployment location, P1 (fig. 1 in Egan et al. 2020*b*), which was equipped with several physical oceanographic sensors to quantify near-bed forcing, and a suite of optical instrumentation for particle characterization.

Relevant physical data were collected from acoustic Doppler velocimeters (ADVs), which were deployed with sensing volumes at 5 and 15 cm above the bed (cmab). The ADVs sampled at 8 Hz for 12 min every hour. ADV data included pressure, 3D current velocity (*u*, *v*, and *w*), and acoustic backscatter (ABS). An acoustic Doppler current profiler (ADP), bottom pressure recorder, and conductivity–temperature–depth sensor (CTD) provided ancillary depth-resolved current velocity, wave statistics, and CTD data, respectively.

The optical measurement platform consisted of two Laser In Situ Scattering and Transmissometry sensors (LISST-100X, type C), two spectral absorption-attenuation meters (ac-9 and ac-s; 10 and 25 cm path lengths, respectively), and two backscattering sensors (ECObb) mounted at 15 and 45 cmab. We present data collected at 15 cmab, with the exception of backscattering data at 45 cmab collected during W19 when the ECObb at 15 cmab had failed. The LISST measured volume size distribution of particles between 3 and 460 μm (Agrawal and Pottsmith 1994; Agrawal and Mikkelsen 2009). Relevant optical properties from the ac-9 were spectral absorption, $a_{pg}(\lambda)$, attenuation, $c_{pg}(\lambda)$, and scattering coefficients, $b_p(\lambda)$, at nine wavelengths between 400 and 750 nm (the subscript "pg" denotes particulate plus dissolved fractions and λ denotes wavelength). The particulate backscattering coefficient at 660 nm wavelength, $b_{bp}(660)$, was derived from the ECObb.

Physical forcing

ADV data at 5 cmab were rotated into major and minor directions of the tidal ellipse that were estimated from the first and second principal components of the depth-averaged ADP mean velocity time series for each deployment. Here, we denote the major velocity component by *u* and the minor component by *v*, and *w* denotes the vertical component. Each velocity component was decomposed as:

$$u = \overline{u} + \widetilde{u} + u', \tag{1}$$

where the overbar indicates burst-averaged, $\widetilde{u}$ is the wave velocity, and u' represents the turbulent fluctuations in velocity.

We derived combined current and wave shear stress over the periods of the three field experiments following:

$$\tau_{c+w} = \rho u_*^2, \tag{2}$$

where ρ is the density of seawater, determined from CTD measurements, and u_* is friction (or shear) velocity, determined as:

$$u_* = \sqrt{\left| -\overline{u'w'} - \overline{\widetilde{u}\widetilde{w}} \right|}. \tag{3}$$

In Eq. 3, $\overline{u'w'}$ and $\overline{\widetilde{u}\widetilde{w}}$ represent the turbulent Reynolds stress and wave momentum flux, respectively (overbars denote averages). The decomposition was performed following the phase method of Bricker and Monismith (2007).

Particle characteristics

Suspended particle characteristics, co-located with ADV measurements at P1, were derived from in situ optical properties. We define characteristic particle size as the median particle diameter, D_{50}, derived from the LISST-measured particle size distributions (PSDs) at 15 cmab. Estimates of optically derived particle concentration were obtained through a two-step process: (1) log-linear regression between ADV-measured ABS and suspended sediment concentration (SSC), where water samples collected from the P1 study site were used to calibrate the ADV ABS in the laboratory across varying concentrations (details can be found in Egan et al. 2020*a*), and (2) linear regression between ABS-derived SSC and $b_{bp}(660)$.

Particle composition was inferred from the bulk refractive index of particles, n_p, which was derived from optical properties. The parameter, n_p, is described in terms of the particulate backscattering ratio, $\tilde{\boldsymbol{b}}_{\mathbf{bp}}(\mathbf{660})$, and the hyperbolic (Junge-like) slope of the PSD, γ (Twardowski et al. 2001):

$$n_p = 1 + \tilde{\boldsymbol{b}}_{bp}(660)^{0.5377+0.4867}\gamma^2\left(1.4676 + 2.2950\gamma^2 + 2.3113\gamma^4\right), \quad (4)$$

where

$$\tilde{\boldsymbol{b}}_{bp}(660) = \frac{b_{bp}(660)}{b_p(660)}. \quad (5)$$

The variable $b_{bp}(660)$ is obtained from ECObb measurements and $b_p(660)$ is total particulate scattering determined from ac-9 measurements. The parameter γ (Eq. 4) represents the slope of the particulate attenuation spectrum, derived from ac-9 measurements of attenuation and modeled partitioned spectral absorption (Roesler et al. 1989) and has been shown to be related to the hyperbolic distribution of the PSD (Boss et al. 2001*a*,*b*). Oceanic particle values of n_p range between 1.0 and 1.26 (relative to seawater) and give an indication of the composition of particles. Lower values of n_p typically represent less dense particles (e.g., organic) and higher values generally indicate denser particles (e.g., inorganic) (Aas 1996; Lide 1997).

Observations

The South SF Bay field experiment site has been described extensively by Lacy et al. (1996), Brand et al. (2010), Egan et al. (2019, 2020*a*,*b*, 2021) in terms of wave- and current-driven flows, sediment properties, and benthic characteristics. For our study, wind speeds, provided by the National Oceanic and Atmospheric Administration National Data Buoy Center Station RTYC1—9414523—Redwood City, California, peaked at approximately 12 m s^{-1}, with mean wind speeds of 3.7, 2.2, and 3.3 m s^{-1} in S18, W19, and Sp19. Depth-averaged tidal currents were on average 20 cm s^{-1} in the northwest (ebb) to southeast (flood) directions over the field experiments. Wind waves were commonly observed at the site, with wave frequencies in the range of 0.2–0.5 Hz across seasons. Combined current and wave shear stress ranged from negligible to maximum values of approximately 0.75 Pa during S18 and 0.60 Pa during Sp19, and to 2.75 Pa during W19, with mean values of approximately 0.13 Pa across the three seasons (Fig. 1a). These physical site characteristics are largely consistent with those reported by Brand et al. (2010) and Allen et al. (2019; data from North SF Bay).

Suspended particle characteristics, where comparable, were also consistent with previous studies conducted in SF Bay (Brand et al. 2010; Allen et al. 2019). SSC values were similar to those found by Brand et al. (2010); mean values were approximately 25 mg L^{-1} over the seasons. SSC ranged from 16 to 136 mg L^{-1}, peaking during a Sp19 storm (Fig. 1c). Median particle diameter, D_{50}, varied between 17.6 μm during W19 to maximum diameters > 310 μm in biologically productive Sp19. The mean value of D_{50} was hence largest (165.5 μm) in Sp19 and approximately 70–76 μm in S18 and W19 (Fig. 1b). The bulk refractive index of particles provides an indication of particle composition across the field experiments, and ranged from $n_p = 1.04$ to $n_p > 1.8$. Overall, n_p was highest during W19 (mean value of 1.19) and most variable in Sp19 (Fig. 1d). This indicates more minerogenic material in W19 and dynamic changes in particle composition in Sp19, particularly in May.

Relationships between near-bed shear stress and suspended particle processes can be described qualitatively based on field observations. Data collected over the three seasons exhibited shorter (tidal to diurnal) timescale variability in τ_{c+w}, D_{50}, and at times, n_p. Transient events for each season are summarized as follows:

- S18: No discernible transient events. Tidal and advective processes appeared to dominate variability in physical forcing and particle characteristics.
- W19: One major storm event was observed (21 Jan 2019); storm-driven increases in τ_{c+w} were correlated with slight decreases in D_{50}, and large increases in SSC and n_p, that is, increased concentrations of denser (more minerogenic) material, which is evidence for sediment resuspension.
- Sp19: A storm on 21 Apr 2019 resulted in a moderate increase in τ_{c+w}, increased SSC, and large reduction in D_{50}, which suggests particle disaggregation processes.

Variability in near-bed shear stress, particle characteristics, and their relationships exhibited similarities and differences across the seasons, which led us to pose the following:

1. Seasonally, which particle characteristics were most sensitive to variability in near-bed forcing processes?
2. Can we derive τ_{char}, the shear stress at which particles begin to resuspend or disaggregate, from in situ acoustic and optical measurements; and how do these τ_{char} values compare to τ_{cr} determined for similar environments?

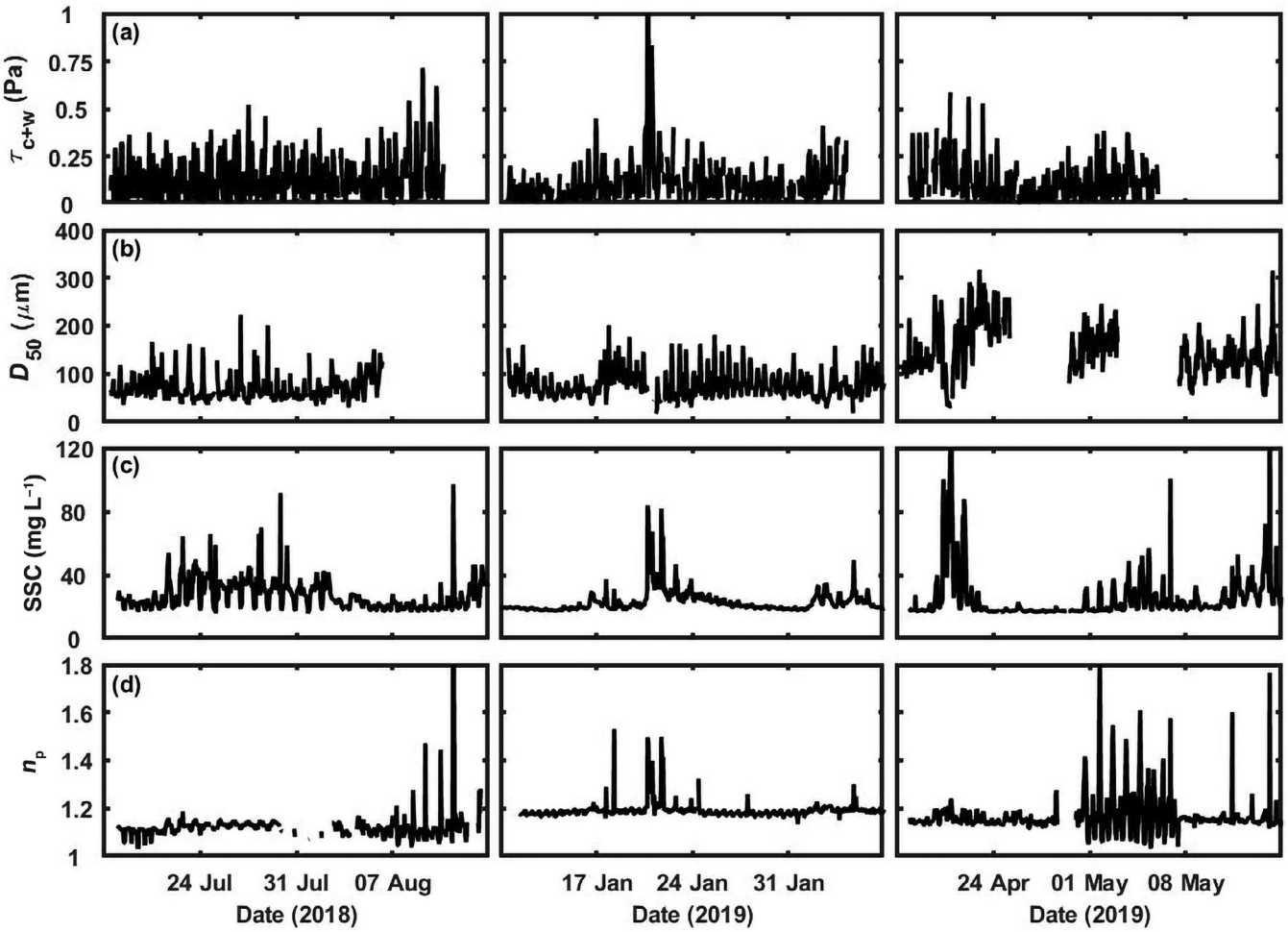

Fig. 1. Time series of (**a**) combined current and wave shear stress, (**b**) D_{50}, (**c**) SSC, and (**d**) bulk index of refraction of particles, n_p (Eq. 4) for S18 (left column), W19 (middle column), and Sp19 (right column). Data in (**a**–**d**) were derived from in situ measurements.

Results and discussion

We first provide answers to these questions, and then describe novel acoustic and optical data analysis methods that enabled us to reach these conclusions.

1. Seasonal variability in SF Bay resulted in different particle characteristics that were most sensitive to hydrodynamic processes:
   - Particle composition in S18
   - Particle concentration in W19
   - Particle size in Sp19.
2. Yes, τ_{char} can be derived from in situ acoustic and optical measurements collected in South SF Bay, and these values are largely consistent with values reported in the literature for cohesive sediments:
   - $\tau_{char} = 0.125$ Pa in S18.
   - $\tau_{char} = 0.05$ Pa in W19.
   - $\tau_{char} = 0.25$ Pa in Sp19.

We investigated the relationships between τ_{c+w} and suspended particle characteristics over the three seasons by normalizing D_{50}, SSC, and n_p by their means, and exploring each parameter's variability with τ_{c+w} (Fig. 2). We observed that the slope of the regression between normalized particle characteristics and τ_{c+w} oftentimes changed at particular values of τ_{c+w}. The magnitude of slope change varied and occurred at different values of τ_{c+w} depending on the characteristic itself as well as the season (Fig. 2). Therefore, we hypothesized that τ_{char} could be determined based on the τ_{c+w} at which the maximum percent slope change occurred, and that the magnitude of percent change in slope may indicate the particle characteristics that are most sensitive to variability in near-bed shear stress. Essentially, we used regression slopes as the statistical parameter in a change point analysis of shear stress-ordered data.

To examine this hypothesis, we assumed a value of τ_{char} between 0.025 and 0.3 Pa (iterating by steps of 0.025 Pa), and

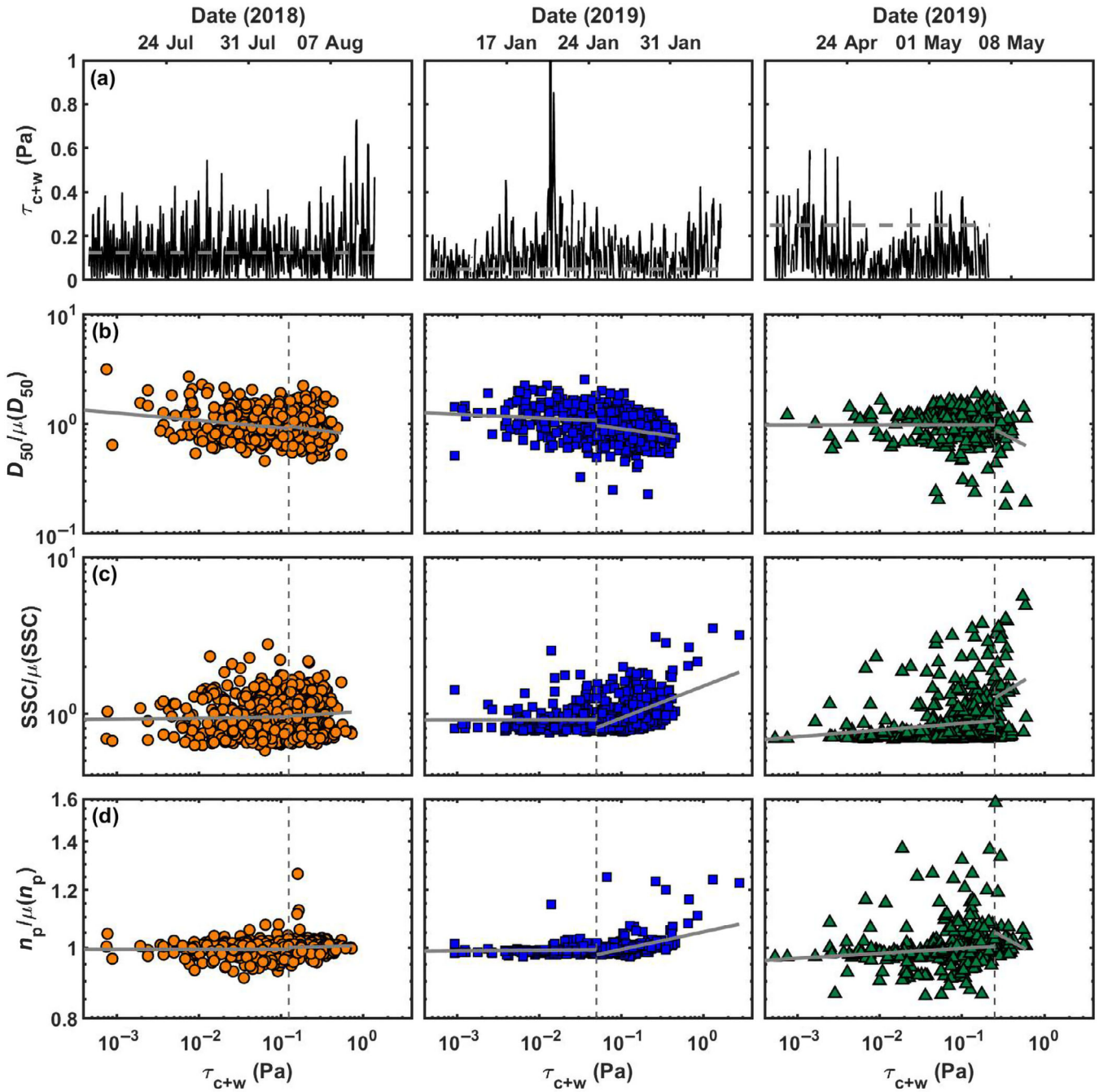

Fig. 2. (**a**) Time series of τ_{c+w}. (**b–d**) Suspended particle characteristics, normalized by their mean, as a function of τ_{c+w} for (**b**) D_{50}, (**c**) SSC, and (**d**) n_p, in log-space, for S18 (left; orange), W19 (middle; blue), and Sp19 (right; geen). Dashed, gray lines represent values of τ_{char} for each season. Solid, gray lines in (**b–d**) are the least-squares regression lines for data below and above τ_{char}.

calculated the slope of the least-squares regression between normalized D_{50}, SSC, and n_p and τ_{c+w} for data less than and greater than $\tau_{char\_assumed}$, where, for example, $m\text{SSC}_A$ is the slope of the regression between normalized SSC and τ_{c+w} for data less than $\tau_{char\_assumed}$ and $m\text{SSC}_B$ is the slope of the regression between normalized SSC and τ_{c+w} for data greater than $\tau_{char\_assumed}$ (in log-space). We performed this analysis across the seasons. We then calculated the absolute fractional slope change from A to B, following:

$$\%\Delta m[D_{50}] = \left|\frac{(mD_{50_B} - mD_{50_A})}{mD_{50_A}}\right|, \tag{6a}$$

Table 1. Absolute fractional slope change, $\%\Delta m$ (Eq. 6). The largest values for each particle characteristic and each season are highlighted in boldface.

τ_{char} (Pa)	$\%\Delta m[D_{50}]$			$\%\Delta m$[SSC]			$\%\Delta m[n_p]$		
	S18	W19	Sp19	S18	W19	Sp19	S18	W19	Sp19
0.025	0	**4.57**	5.94	3.98	17.1	11.7	2.98	9.26	36.6
0.050	0	2.14	13.9	**5.44**	**365**	4.80	3.74	21.9	24.9
0.075	0	0.21	31.7	2.99	63.6	17.3	19.3	16.6	**517**
0.100	0.04	0	17.9	3.50	137	14.0	18.6	31.5	10.4
0.125	0.39	0	41.1	3.89	87.7	**22.7**	**152**	**46.4**	5.92
0.150	0.91	0	29.7	0	39.2	16.6	0	46.0	3.79
0.175	1.73	0.21	31.8	0	25.4	17.8	2.60	44.4	1.56
0.200	1.17	0.11	106	0	22.8	16.1	1.10	39.7	0
0.225	0.69	0.36	69.9	0	20.6	12.0	2.38	39.6	0
0.250	**1.80**	1.44	**642**	0	19.1	6.34	0	37.0	0
0.275	0	0.30	142	0	18.5	4.06	0	34.1	0
0.300	0	0.38	0	0	18.3	6.69	0	34.3	1.94

$$\%\Delta m[\mathrm{SSC}] = \left|\frac{(m\mathrm{SSC}_B - m\mathrm{SSC}_A)}{m\mathrm{SSC}_A}\right|, \quad (6b)$$

$$\%\Delta m[n_p] = \left|\frac{(mn_{p_B} - mn_{p_A})}{mn_{p_A}}\right|, \quad (6c)$$

In cases where mD_{50} increased with increasing τ_{c+w} or mSSC and mn_p decreased with increasing τ_{c+w}, $\%\Delta m$ was set to zero because here, we are only concerned with effects of increasing shear stress on particle disaggregation and increases in concentration and bulk density.

Results indicated that size effects were more pronounced in Sp19; $\%\Delta m[D_{50}]$ values were orders of magnitude higher than in S18 and W19 (Table 1). Concentration effects were important in W19 and Sp19. However, $\%\Delta m$[SSC] values were oftentimes orders of magnitude higher in W19 at $\tau_{char\_assumed} < 0.125$ Pa, compared with the other two seasons. Seasonal variability in particle composition was less pronounced, with $\%\Delta m[n_p] > 100$ during S18 and Sp19; however, overall, $\%\Delta m[n_p]$ was highest during W19 over the range of $\tau_{char\_assumed}$ (Table 1).

We created ternary diagrams with $\%\Delta m[D_{50}]$, $\%\Delta m$[SSC], and $\%\Delta m[n_p]$ over the range of $\tau_{char\_assumed}$ as inputs to visualize and assess seasonal responses of particle size, concentration, and composition at 15 cmab to $\tau_{char\_assumed}$ (Fig. 3a–c). Briefly, ternary diagrams depict the ratios of three variables as positions on a triangle, where the edges of the triangle are the axes (Howarth 1996). Results for S18 indicate that as $\tau_{char\_assumed}$ increased from 0.025 to 0.125 Pa, particle responses shifted from concentration-dominated to composition-dominated. At $\tau_{char\_assumed} > 0.125$ Pa and $\tau_{char\_assumed} < 0.25$ Pa, particle composition effects became less important relative to particle size. Particle disaggregation processes dominated at $\tau_{char\_assumed}$ of 0.25 Pa in S18 (Fig. 3a). Similar to S18, W19 particle concentration effects decreased with increasing $\tau_{char\_assumed}$, from 0.025 to 0.125 Pa. Above 0.125 Pa, particle composition effects became more important (Fig. 3b). Particle disaggregation processes were relatively unimportant at all values of $\tau_{char\_assumed}$ in W19. Sp19 results differed from the other two seasons in that particle concentration effects were minor over all values of $\tau_{char\_assumed}$ except 0.3 Pa. For $\tau_{char\_assumed}$ less than 0.125 Pa, particle composition effects dominated. Particle size effects became increasingly important with increasing $\tau_{char\_assumed}$, to 0.275 Pa (Fig. 3c).

The $\tau_{char\_assumed}$ values at which we found maximum fractional slope changes in particle characteristics were generally consistent across seasons (Table 1). The largest changes in $\%\Delta m[D_{50}]$ occurred at relatively high shear stress ($\tau_{char\_assumed} = 0.25$ Pa in S18 and Sp19), except during W19 ($\tau_{char\_assumed} = 0.025$ Pa). The largest fractional slope changes in $\%\Delta m$[SSC] were mostly found at relatively low shear stress ($\tau_{char\_assumed} = 0.05$ Pa in S18 and W19, and 0.125 Pa in Sp19), and $\%\Delta m[n_p]$ changes were greatest at moderate shear stress ($\tau_{char\_assumed} = 0.125$ Pa in S18 and W19, and 0.075 Pa in Sp19). Therefore, we defined τ_{char} as the shear stress at which particle characteristics were collectively the most affected for each season. This was determined by summing $\%\Delta m[D_{50}]$, $\%\Delta m$[SSC], and $\%\Delta m[n_p]$ across each value of $\tau_{char\_assumed}$. The value at which the sum of $\%\Delta m$ values was greatest was defined as τ_{char}. Results for each season are:

- $\tau_{char} = 0.125$ Pa in S18,
- $\tau_{char} = 0.05$ Pa in W19,
- $\tau_{char} = 0.25$ Pa in Sp19.

These values of τ_{char} are consistent with typical τ_{cr} values as reported for cohesive sediments (van Rijn 2020), including

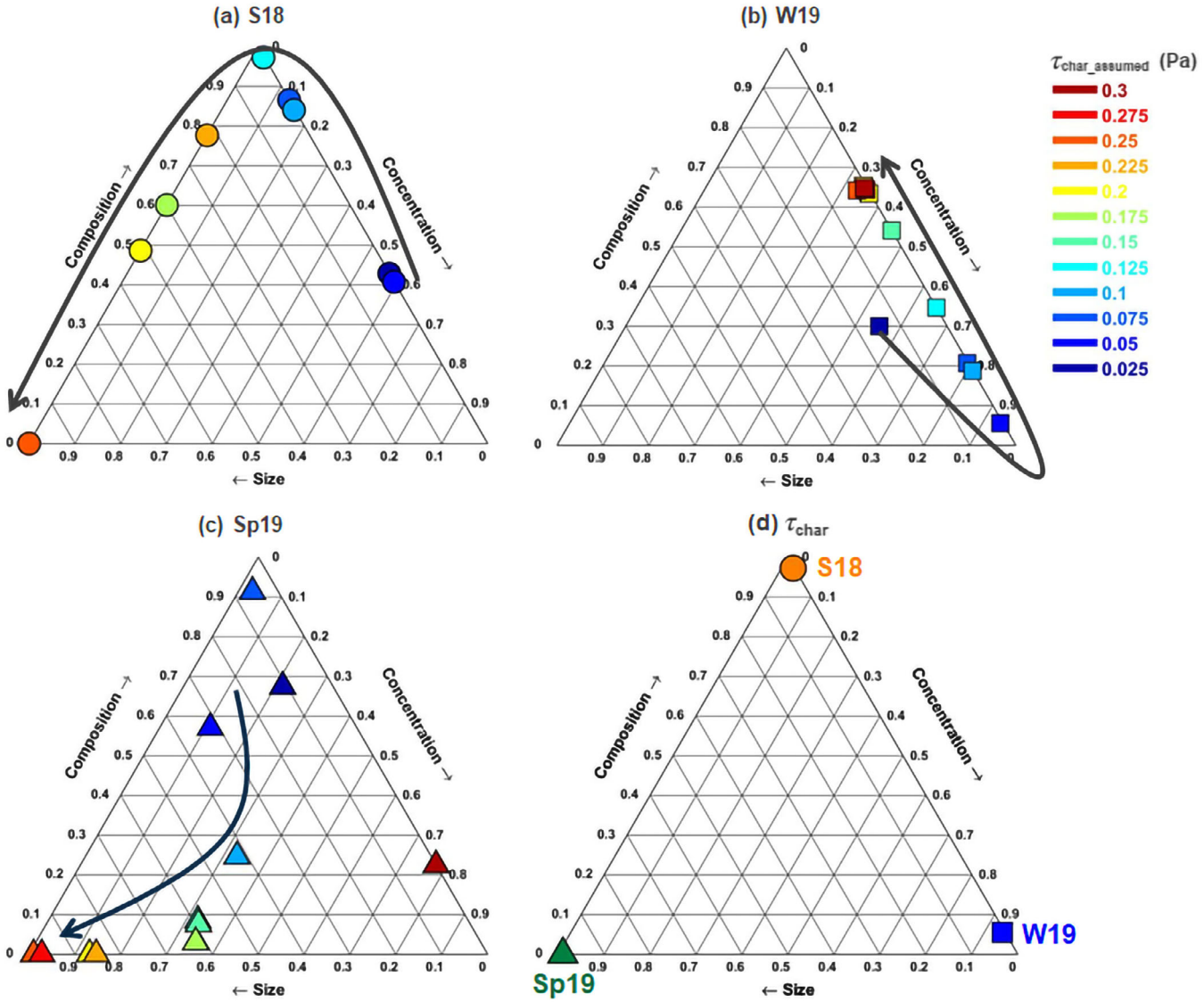

Fig. 3. Ternary diagrams for three different particle characteristics (**a**) in S18, (**b**) in W19, and (**c**) in Sp19 over the range of $\tau_{char\_assumed}$ (legend at upper right; Table 1), and (**d**) at τ_{char} values of 0.125, 0.05, and 0.25 Pa for S18 (orange), W19 (blue), and Sp19 (green).

those found in SF Bay (Partheniades 1965). Egan et al. (2020*a*, *b*) reported τ_{cr} of 0.18 Pa, derived from SEDflume (McNeil et al. 1996; Roberts et al. 1998) analysis of cores collected at the experiment site in S18. Allen et al. (2019) presented seasonal variability in τ_{cr} that ranged between negligible to approximately 0.2 Pa in San Pablo Bay (North SF Bay), California, with the lowest values observed in the winter. Brand et al. (2010) reported τ_{cr} equal to 0.1 Pa for the shallow eastern shoals of SF Bay. Our S18 τ_{char} value of 0.125 Pa is equivalent to a typical τ_{cr} of mudflats, as reported by Williamson and Ockenden (1996), Maa et al. (1998), and Shi et al. (2015). The lower τ_{char} (0.05 Pa) determined for W19 is comparable to the τ_{cr} value reported for fluff layer resuspension (Maa et al. 1998; Wang 2003; El Ganaoui et al. 2004; Schaaff et al. 2006; Mathew and Winterwerp 2017). The highest τ_{char}, 0.25 Pa, determined for Sp19, is a typical τ_{cr} of a weakly consolidated mud bed (Tolhurst et al. 2000; Le Hir et al. 2008), and tidal channels with a dynamic bed consisting of low-density mud (Jones and Jaffe 2013; van Rijn 2020).

Conclusions

Novel analysis of in situ acoustic and optical data collected near-bed, in a shallow, wave- and current-driven environment enabled determination of (1) particle characteristics that were most sensitive to near-bed physical forcing over seasonal

scales and (2) the characteristic shear stress at which changes to particle characteristics were greatest. The most sensitive particle characteristics at the identified values of τ_{char} for all seasons together, are shown in Fig. 3d. Changes in particle composition that were observed to be of most importance in S18 can be driven by a number of physical processes, including sediment resuspension, particle disaggregation, and advection, in addition to biological processes. Relationships between τ_{c+w} and particle characteristics suggest that each of these processes likely played a role in modulation of particle characteristics in S18. In W19, particle concentration effects were most affected at τ_{char} of 0.05 Pa, suggesting fluff layer resuspension processes dominated over this period. Particle disaggregation processes were most important during the biologically productive Sp19 period, with initial disaggregation occurring at $\tau_{char} = 0.25$ Pa. These results suggest that it may be more important to parameterize τ_{char}, as opposed to τ_{cr}, for sediment transport models, and that τ_{char} can be estimated from acoustic and optical field measurements. While the method here is demonstrated for seasonal relationships between τ_{c+w} and optical proxies representing particle size, concentration, and bulk density, it can be applied to τ_c or τ_w over various time periods to investigate, for example, advective, tidally driven, storm-driven, or diurnal forcing.

References

Aas, E. 1996. Refractive index of phytoplankton derived from its metabolite composition. J. Plankton Res. **18**: 2223–2249. doi:10.1029/2000JC000404

Agrawal, Y. C., and H. C. Pottsmith. 1994. Laser diffraction particle sizing in STRESS. Cont. Shelf Res. **14**: 1101–1121. doi:10.1016/0278-4343(94)90030-2

Agrawal, Y. C., and O. A. Mikkelsen. 2009. Empirical forward scattering phase functions from 0.08 to 16 deg. for randomly shaped terrigenous 1–21mm sediment grains. Opt. Express **17**: 8805–8814. doi:10.1364/OE.17.008805

Allen, R. M., J. R. Lacy, M. T. Stacey, and E. A. Variano. 2019. Seasonal, spring-neap, and tidal variation in cohesive sediment transport parameters in estuarine shallows. J. Geophys. Res. Oceans **124**: 7265–7284. doi:10.1029/2018JC014825

Boss, E., M. S. Twardowski, and S. Herring. 2001*a*. Shape of the particulate beam attenuation spectrum and its inversion to obtain the shape of the particulate size distribution. Appl. Optics **40**: 4885–4893. doi:10.1364/AO.40.004885

Boss, E., W. S. Pegau, W. D. Gardner, J. R. V. Zaneveld, A. H. Barnard, M. S. Twardowski, G. C. Chang, and T. D. Dickey. 2001*b*. Spectral particulate attenuation and particle size distribution in the bottom boundary layer of a continental shelf. J. Geophys. Res. **106**: 9509–9516. doi:10.1029/2000JC900077

Brand, A., J. R. Lacy, K. Hsu, D. Hoover, S. Gladding, and M. T. Stacey. 2010. Wind-enhanced resuspension in the shallow waters of South San Francisco Bay: Mechanisms and potential implications for cohesive sediment transport. J. Geophys. Res. Oceans **115**: C11024. doi:10.1029/2010JC006172

Bricker, J. D., and S. G. Monismith. 2007. Spectral wave-turbulence decomposition. J. Atmos. Oceanic Tech. **24**: 1479–1487. doi:10.1175/JTECH2066.1

Egan, G., M. Cowherd, O. Fringer, and S. Monismith. 2019. Observations of near-bed shear stress in a shallow, wave- and current-driven flow. J. Geophys. Res. Oceans **124**: 6323–6334. doi:10.1029/2019JC015165

Egan, G., A. J. Manning, G. Chang, O. Fringer, and S. Monismith. 2020*a*. Sediment-induced stratification in an estuarine bottom boundary layer. J. Geophys. Res. Oceans **125**: e2019JC016022. doi:10.1029/2019JC016022

Egan, G., G. Chang, G. Revelas, S. Monismith, and O. Fringer. 2020*b*. Bottom drag varies seasonally with biological roughness. Geophys. Res. Lett. **47**: e2020GL088425. doi:10.1029/2020GL088425

Egan, G., G. Chang, S. McWilliams, G. Revelas, O. Fringer, and S. Monismith. 2021. Cohesive sediment erosion in a combined wave-current boundary layer. J. Geophys. Res. Oceans **126**: e2020JC016655. doi:10.1029/2020JC016655

El Ganaoui, O., E. Schaaff, P. Boyer, M. Amielh, F. Anselmetc, and C. Grenz. 2004. The deposition and erosion of cohesive sediments determined by a multi-class model. Estuar. Coast. Shelf Sci. **60**: 457–475. doi:10.1016/j.ecss.2004.02.006

Howarth, R. J. 1996. Sources for a history of the ternary diagram. Br. J. Hist. Sci. **29**: 337–356. doi:10.1017/S000708740003449X

James, S. C., C. A. Jones, M. D. Grace, and J. D. Roberts. 2010. Advances in sediment transport modeling. J. Hydraul. Res. **48**: 754–763. doi:10.1080/00221686.2010.515653

Jones, C. A., and B. E. Jaffe. 2013. Influence of history and environment on the sediment dynamics of intertidal flat. Mar. Geol. **345**: 294–303. doi:10.1016/J.MARGEO.2013.05.011

Lacy, J. R., Schoelhamer, D. H., & Burau, J. R. (1996), Suspended-solids flux at a shallow-water site in South San Francisco Bay, California. In: *Proceedings of the North American Water and Environment Congress '96*, American Society of Civil Engineers, New York.

Le Hir, P., P. Cann, B. Waeles, J. Jestin, and P. Bassoullet. 2008. Erodibility of natural sediments: experiments on sand/mud mixtures from laboratory and field erosion tests. In *Proceedings of Marine Science* (pp. 137–153). Intercoh 2005. Saga, Japan. doi:10.1016/S1568-2692(08)80013-7

Lick, W. 2009, *Sediment and contaminant transport in surface waters*. Boca Raton, FL: CRC Press.

Lide, D. R. [ed.]. 1997, *Physical and optical properties of minerals*. CRC handbook of chemistry and physics, 77th Edition. Boca Raton, FL: CRC Press.

Maa, J. P. -Y., L. Sanford, and J. P. Halka. 1998. Sediment resuspension characteristics in Baltimore Harbor, Maryland. Mar. Geol. **146**: 137–145. https://doi.org/10.1016/S0025-3227(97)00120-5

Mathew, R., and J. C. Winterwerp. 2017. Surficial sediment erodibility from time-series measurements of suspended sediment concentrations: Development and validation. Ocean Dyn. **67**: 691–712. https://doi.org/10.1007/s10236-017-1055-2

McNeil, J., C. Taylor, and W. Lick. 1996. Measurements of erosion of undisturbed bottom sediments with depth. J. Hydraul. Eng. **122**: 316–324. https://doi.org/10.1061/(ASCE)0733-9429(1996)122:6(316)

Partheniades, E. 1965. Erosion and deposition of cohesive soils. J. Hydraul. Div. **91**: 105–139.

Roberts, J., R. Jepsen, D. Gothard, and W. Lick. 1998. Effects of particle size and bulk density on erosion of quartz particles. J. Hydraul. Eng. **124**: 1261–1267. https://doi.org/10.1061/(ASCE)0733-9429(1998)124:12(1261)

Roesler, C. S., M. J. Perry, and K. L. Carder. 1989. Modeling in situ phytoplankton absorption from total absorption spectra in productive inland marine waters. Limnol. Oceanogr. **34**: 1510–1523. https://doi.org/10.4319/lo.1989.34.8.1510

Schaaff, E., C. Grenz, C. Pinazo, and B. Lansard. 2006. Field and laboratory measurements of sediment erodibility: A comparison. J. Sea Res. **55**: 30–42. doi:10.1016/j.seares.2005.09.004

Shi, B., Y. P. Wang, Y. Yang, M. Li, P. Li, W. Ni, and J. Gao. 2015. Determination of critical shear stress for erosion and deposition based on *in situ* measurements of currents and waves over an intertidal mudflat. J. Coast. Res. **31**: 1344–1356. doi:10.2112/JCOASTRES-D-14-00239.1

Tolhurst, T. J., R. Riethmueller, and D. M. Paterson. 2000. In-situ versus laboratory analysis of sediment stability from intertidal mudflats. Cont. Shelf Res. **20**: 1317–1334. doi:10.1016/S0278-4343(00)00025-X

Twardowski, M. S., E. Boss, J. B. Macdonald, W. S. Pegau, A. H. Barnard, and J. R. V. Zaneveld. 2001. A model for estimating bulk refractive index from the optical backscattering ratio and the implications for understanding particle composition in case I and case II waters. J. Geophys. Res. **106**: 14,129–14,142. doi:10.1029/2000JC000404

Van Rijn, L. C. (2020), Literature review of critical bed-shear stresses for mud-sand mixtures. Technical Note. www.leovanrijn-sediment.com

Wang., Y. H. 2003. The intertidal erosion rate of cohesive sediment: A case study from Long Island sound. Estuar. Coast. Shelf Sci. **56**: 891–896. doi:10.1016/S0272-7714(02)00215-9

Williamson, H. J., and M. C. Ockenden. 1996. ISIS: An instrument for measuring erosion shear stress *in situ*. Estuar. Coast. Shelf Sci. **42**: 1–18. https://doi.org/10.1006/ecss.1996.0001

Winterwerp, J. C., W. G. M. Van Kesteren, B. Van Prooijen, and W. Jacobs. 2012. A conceptual framework for shear flow-induced erosion of soft cohesive sediment beds. J. Geophys. Res. Oceans **117**: C10020. https://doi.org/10.1029/2012JC008072

Acknowledgments

This work was funded by the National Science Foundation under grant OCE-1736668. We wish to extend our gratitude to Kara Scheu, Marianne Cowherd, Stephen LaMothe, and Jim Christmann for their assistance in the field.

Submitted 14 June 2021
Revised 01 October 2021
Accepted 07 October 2021